Frequency-Based Energy-Management Strategy for Stand-Alone Systems With Distributed Battery Storage

Andoni Urtasun, *Student Member, IEEE*, Ernesto L. Barrios, *Student Member, IEEE*, Pablo Sanchis, *Senior Member, IEEE*, and Luis Marroyo, *Member, IEEE*

***Abstract*—Distributed generation is an attractive solution for stand-alone ac supply systems. In such systems, the installation of two or more energy-storage units is recommended for system redundancy and may also be required when there is a consumption increase following installation. However, energy management with multiple energy-storage units has been, but vaguely analyzed in the literature and the few studies made are based on communication cables with a central supervisor. This paper proposes an energy-management strategy for a multiple-battery system which makes it possible to avoid the use of communication cables, rendering the system more cost effective and reliable. The strategy modifies the conventional droop method so that the power becomes unbalanced, allowing for the regulation of one or more battery voltages or currents, as required. Furthermore, whenever the frequency is high, the PV inverters reduce their power in order to prevent the battery from overcharge or high charging currents. On the other hand, whenever the frequency is low, then either the noncritical loads are regulated or the system stops in order to prevent the battery from overdischarge or high discharging currents. Simulation and experimental validation are performed for a system with two-battery inverters, two-PV inverters, and a number of loads.**

***Index Terms*—Batteries, distributed generation, droop control, energy management, hybrid system, microgrids, photovoltaic (PV) power, stand-alone system.**

I. Introduction

FOR remote locations with difficult access to the power grid, stand-alone systems are more cost effective. In fact, these systems are widely established in hilly regions and remote villages, where they are used for a wide range of applications such as rural electrification, auxiliary power units for emergency services or military applications, and manufacturing facilities using sensitive electronics [1], [2].

Distributed generation may be an attractive solution for stand-alone ac supply systems [3], [4]. A frequently adopted and sustainable solution consists of installing photovoltaic (PV) and wind generation with battery energy storage [5]–[7]. In this system, shown in Fig. 1, ac/ac converters are used to connect the wind turbines (WTs) to the ac grid, while the batteries and PV generators are connected using dc/ac inverters [8], [9].

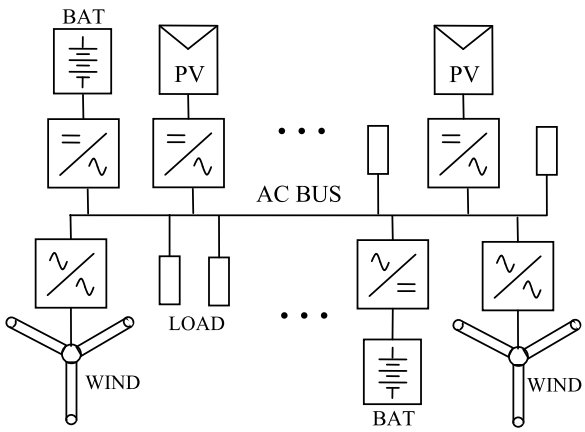

Fig. 1. Stand-alone hybrid system with distributed energy storage and generation.

This system requires high-quality energy management for optimal operation. In normal operation, the renewable-energy-sources (RES) function under maximum power point tracking (MPPT), and the batteries offset the difference between consumption and generation. In this situation, it is advantageous to make the battery inverters operate under voltage-control mode using droop methods, thereby making the inverters independent and avoiding communication between them, for a more cost effective and reliable system [10]–[12]. For their part, the PV/wind converters harvest the solar/wind energy and operate under current-control mode injecting power to the grid [13], [14]. In this operating mode, the state-of-charge (SOC) of the energy storage systems changes according to the difference between consumption and generation. Then, when the batteries are fully charged and generation is higher than consumption, the RES power should be limited in order to protect the batteries from overcharging [15]. Similarly, if the charging current exceeds its maximum value, then the RES power should also be reduced in order to provide overcurrent protection. On the contrary, when the batteries are fully discharged and consumption is higher than generation or if the discharging current exceeds its maximum value, the loads should be disconnected or the system should be shutdown in order to prevent serious damage to the batteries.

Some authors have implemented this energy-management strategy for islanded ac microgrids with only one battery bank.

Manuscript received May 2, 2014; revised September 2, 2014; accepted October 13, 2014. Date of publication October 23, 2014; date of current version April 15, 2015. This work was supported in part by the Spanish Ministry of Economy and Competitiveness under Grant DPI2013-42853-R and by the Public University of Navarre through a doctoral scholarship. This work was also supported by the INGETEAM POWER TECHNOLOGY. Recommended for publication by Associate Editor M. Liserre.

The authors are with the Department of Electrical and Electronic Engineering, Public University of Navarra, 31006 Pamplona, Spain (e-mail: andoni.urtasun@unavarra.es; pablo.sanchis@unavarra.es; luisma@unavarra.es).

Color versions of one or more of the figures in this paper are available online at http://ieeexplore.ieee.org.

Digital Object Identifier 10.1109/TPEL.2014.2364861

The most complicated part of the control consists of regulating the battery overcharge voltage or the maximum charging current yet with no communication cables between the distributed inverters. While in some works, a central supervisor is required for the energy management [16], [17], other authors completely avoid the communication system by using the grid frequency as a communication signal [13], [18], [19]. In [13], an integral term is added to the conventional droop method in order to increase or decrease the frequency. The frequency is used by the RES and the battery to switch from voltage-control mode to power-control mode and vice versa, making it possible to control the battery power when required in order to regulate the SOC. In [18] and [19], the battery inverter always operates under voltage-control mode and the RES under current-control mode. When the battery is fully charged or the battery current exceeds its maximum value, then the battery inverter increases the frequency as dictated by the PI controller output. This message is detected by the RES converters, which continuously reduce the power generated in order to regulate the battery voltage or current, preventing an overcharge or overcurrent.

An energy-management strategy with multiple battery banks has been vaguely analyzed in the literature. However, the installation of two or more energy-storage units is recommended for system redundancy [20]. It may also be required when there is a consumption increase subsequent to installation [21]. The management of a number of batteries becomes more problematic because, in real applications, their SOC does not evolve simultaneously. As a result, the energy-management strategy must also include some additional controls. Specifically, the voltage of the most charged battery must first be controlled, followed by the voltage of the other batteries and, finally, the voltage of all batteries, all this in an inverter-based system with extremely variable generation and consumption. In [21], a supervisory control for the management of multiple batteries is proposed. Whenever the battery voltages reach their maximum values, the battery inverters switch to current-control mode, while the RES inverters switch to voltage-control mode and generate the dc grid, providing the required power to supply the batteries and the loads. The control also alternates the charging of the various batteries. However, this energy management is possible, thanks to the central supervisor. Furthermore, battery overcurrent protection has not been implemented.

This paper proposes an energy management strategy for a multiple-battery system with no need for communication cables between inverters or with a central supervisor. Whenever the batteries are fully charged or are absorbing too much current, then the grid frequency is increased. This is measured by the RES inverters, which reduce their power in order to control the battery voltages or currents. Furthermore, the control coordinates the various batteries. If some batteries have not reached their maximum voltage or current, then the surplus power is transferred from the charged batteries to the noncharged batteries without limiting the RES power, making the most of the solar/wind energy. This paper also addresses protection during battery discharging. As in the case of battery charging, when the batteries are either fully discharged or are delivering too much current, the grid frequency is decreased. The power is first transferred from some batteries to the others. However, if all the batteries have reached the minimum voltage or maximum discharging current, then the frequency reduction is detected by the less critical loads, which are either regulated or disconnected. If this is not possible, then the system is shutdown in order to prevent irreversible damage to the batteries.

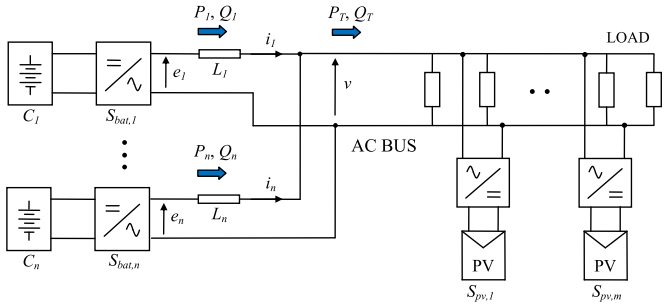

Fig. 2. Battery inverters, PV inverters, and loads connected in parallel.

This paper is organized as follows. Section II presents the proposed energy- management strategy by describing the different converter operation. Section III defines the operating modes resulting from the converter operation and provides some simulation results. In Section IV, small-signal modeling is presented in order to analyze the system stability and dynamic performance. Experimental results are then provided in Section V to verify the proposed strategy. Finally, conclusions of this study are given in Section VI.

II. Proposed Energy-Management Strategy

A. System Description

Fig. 2 represents the stand-alone system shown in Fig. 1, where *n* battery inverters, *m* PV inverters, and a number of loads are connected to the common ac bus. The battery inverters are connected in parallel through the output impedance, formed by the filter inductance and the line impedance. However, since the line impedance is much smaller than the filter impedance, the output impedance can be approximated as the filter inductance L_i. The battery inverter rated powers $S_{\mathrm{bat},i}$, battery capacities C_i, battery real powers P_i, battery reactive powers Q_i, net real power P_T, net reactive power Q_T, PV inverter rated powers $S_{\mathrm{pv},i}$, and instantaneous value of voltages and currents e_i and i_i are also defined in the figure.

In this system, the battery inverters always operate under voltage-control mode using droop methods and generate the grid. For their part, the RES converters operate under current-control mode, injecting either the maximum available power or a power below the MPP into the grid. The operation of the battery inverters, RES converters, and noncritical loads is presented below.

B. Battery Inverter Operation

The droop method is an advantageous grid generation technique with multiple voltage-source inverters, making it possible to share the real and reactive powers in proportion to the inverter ratings with no need for communication. This paper

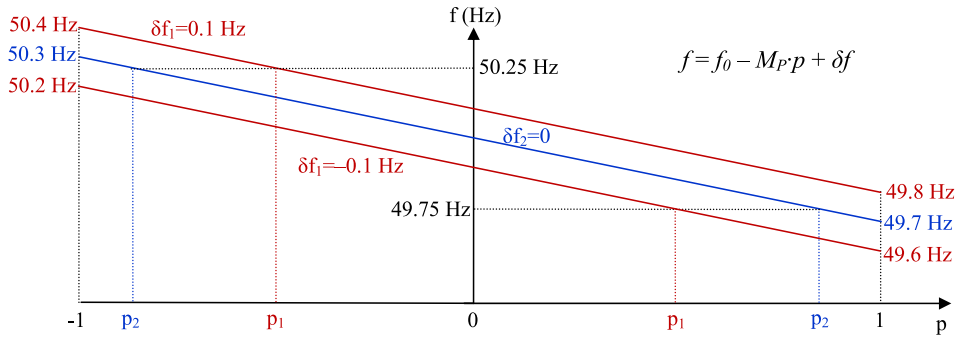

Fig. 3. Proposed $P-f$ curve.

addresses energy management and, therefore, the real power. For this reason, the reactive power droop method is not analyzed here; however, a number of droop methods can be consulted in [22]–[25]. For the sake of clarity, the real power analysis is carried out for two-battery inverters; however, this can be readily generalized for *n* inverters. The conventional droop characteristic is expressed as follows:

$$f = f_0 - M_P \cdot p \tag{1}$$

where f is the inverter frequency, f_0 is the nominal frequency, M_P is the droop coefficient, and $p = P/S_{\text{bat}}$ is the per-unit real power.

In steady-state operation, the inverter frequency is the same for all inverters. Hence, from (1), and setting the same values f_0 and M_P for all inverters, the following is obtained:

$$f_1 = f_2 \Rightarrow p_1 = p_2. \tag{2}$$

In this paper, (1) is used during normal operation, and as a result, the power is shared among the inverters. However, in some situations equal power sharing is not desirable. The proposed strategy then modifies (1) as follows:

$$f = f_0 - M_P \cdot p + \delta f \tag{3}$$

where δf is the shifting frequency and will be changed by the control.

In steady-state operation, from (3), the condition $f_1 = f_2$ leads to

$$f_1 = f_2 \Rightarrow p_1 - p_2 = \frac{\delta f_1 - \delta f_2}{M_P}. \tag{4}$$

This equation shows that adding the term δf results in an unequal power distribution. From (4), if δf_2 and the load are maintained constant, increasing δf_1 results in increasing p_1 and reducing p_2, while reducing δf_1 results in decreasing p_1 and increasing p_2. Taking this into account, if battery 1 reaches its minimum voltage or its maximum discharging current, battery inverter 1 will reduce δf_1 and its power will decrease, preventing overdischarge. On the other hand, if battery 1 becomes fully charged or absorbs an excessive current, then the battery inverter will increase δf_1 and its power will increase. Since the power in charging mode is negative, this will result in a battery current and voltage reduction, preventing overcharge.

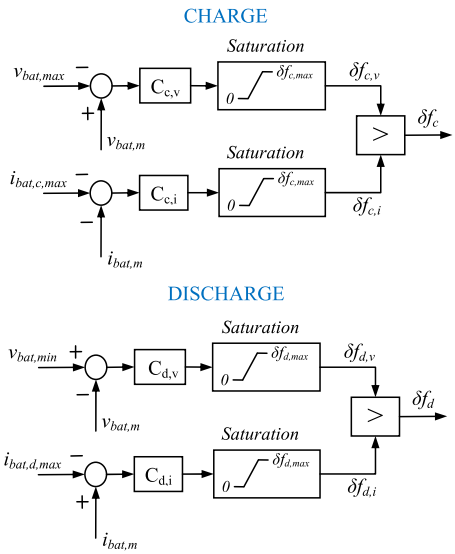

Fig. 4. Calculation of δf_c and δf_d.

This fact can be observed in Fig. 3, where three different $P-f$ curves are shown. The parameters are $f_0 = 50$ Hz, $M_P = 0.3$ Hz for all curves. The curve for inverter 2 has not been modified ($\delta f_2 = 0$), while two modified curves are plotted for inverter 1 ($\delta f_1 = -0.1$ Hz and $\delta \Delta f_1 = 0.1$ Hz). Two operating points have been plotted in the figure, for $P_T > 0$ and for $P_T < 0$. In discharging mode ($P_T > 0$), battery 1 has reduced the shifting frequency to $\delta f_1 = -0.1$ Hz. As a result, inverter 1 delivers less power than inverter 2. On the other hand, in charging mode ($P_T < 0$), battery 1 has increased the shifting frequency to $\delta f_1 = 0.1$ Hz. Thus, inverter 1 absorbs less power than inverter 2.

Although parameters f_0 and M_P are the same for all battery inverters in order to share the per-unit power in normal operation, parameter δf varies as a function of the operating point and is obtained by each battery inverter as

$$\delta f = \delta f_c - \delta f_d \tag{5}$$

where δf_c ($\delta f_c \geq 0$) is the charge shifting frequency, and δf_d ($\delta f_d \geq 0$) is the discharge shifting frequency.

The calculation of δf_c and δf_d is shown in Fig. 4. During charging mode, $\delta f_d = 0$ and $\delta f_c \geq 0$. On the one hand, the

difference between the measured battery voltage, $v_{\mathrm{bat},m}$, and the maximum battery voltage, $v_{\mathrm{bat,max}}$, is entered in controller $C_{c,v}$, which calculates $\delta f_{c,v}$, limited from 0 to $\delta f_{c,\max}$. On the other hand, from the difference between the measured battery current, $i_{\mathrm{bat},m}$ (negative for charging mode), and the maximum battery charging current, $i_{\mathrm{bat},c,\max}$, controller $C_{c,i}$ determines $\delta f_{c,i}$, also limited from 0 to $\delta f_{c,\max}$. Then, the highest value δf_c is selected since it is more restrictive. During discharging mode, $\delta f_c = 0$ and $\delta f_d \geq 0$. In this case, the calculations are similar to the charging mode, but the references are the minimum battery voltage, $v_{\mathrm{bat,min}}$, and the maximum battery discharging current, $i_{\mathrm{bat},d,\max}$. The outputs in this case are $\delta f_{d,v}$ and $\delta f_{d,i}$, the limit value is $\delta f_{d,\max}$, and the highest value δf_d is selected as the most restrictive.

Normally, the battery currents and voltages are within limits, that is, $v_{\mathrm{bat,min}} < v_{\mathrm{bat}} < v_{\mathrm{bat,max}}$ and $-i_{\mathrm{bat},c,\max} < i_{\mathrm{bat}} < i_{\mathrm{bat},d,\max}$. As a result, the controller outputs are saturated to zero, $\delta f_c = 0$, $\delta f_d = 0$, $\delta f = 0$, and expressions (1) and (2) are valid, leading to an equal power distribution. When a battery is fully charged and its voltage exceeds $v_{\mathrm{bat,max}}$ $(v_{\mathrm{bat}} > v_{\mathrm{bat,max}})$, or its charging current exceeds $i_{\mathrm{bat},c,\max}$ $(i_{\mathrm{bat}} < -i_{\mathrm{bat},c,\max})$, then δf is increased, making it possible to reduce the power absorbed by that battery. On the other hand, when the battery is fully discharged and its voltage drops below $v_{\mathrm{bat,min}}(v_{\mathrm{bat}} < v_{\mathrm{bat,min}})$, or its discharging current exceeds $i_{\mathrm{bat},d,\max}(i_{\mathrm{bat}} > i_{\mathrm{bat},d,\max})$, then δf is decreased, resulting in a reduction in the power delivered by that battery.

If there is no variation in generation and consumption, in other words, net power P_T is constant; then, the reduction in the power absorbed (delivered) by one battery leads to an increase in the power absorbed (delivered) by the other battery. As a result, the control presented will be stable if the entire storage system is able to support the net power. However, if all batteries are fully charged or they are absorbing too much current, then all batteries will increase the frequency together. An RES power reduction is then required, which is presented in Section II-C. On the other hand, if all batteries have reached the minimum voltage or maximum discharging current, all batteries will decrease the frequency together. In this case, the noncritical loads should be regulated, as presented in Section II-D.

C. RES Converter Operation

The RES converters operate under current-control mode, injecting power to the grid. They usually perform MPPT and can reduce the power depending on the grid frequency deviation. The grid frequency deviation Δf is defined as

$$\Delta f = f - f_0. \tag{6}$$

Each RES converter measures the frequency and obtains the measured frequency deviation Δf_m. The frequency measurement does not involve an additional cost since this is already included in the RES inverters for grid synchronization and islanding detection. The frequency obtained by the phase-locked loop (PLL) is then filtered in order to avoid noise, transients, and external interferences. A high value is preferred for the filter time constant, τ_f, to prevent transient frequency oscillations

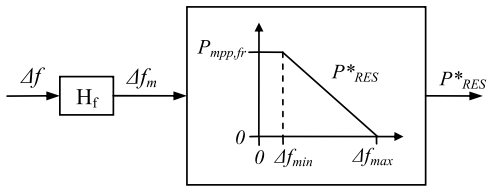

Fig. 5. Calculation of RES power reference $P_{*\mathrm{RES}}$.

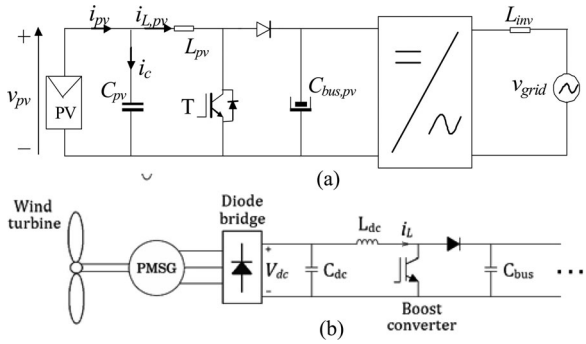

Fig. 6. Renewable-energy-source systems. (a) Single-phase two-stage PV inverter. (b) AC/DC stage of the wind-energy converter.

from reducing the RES power when it is not required. However, a very high value would decrease the control stability margin, and a tradeoff must be balanced. If the measured frequency deviation Δf_m is higher than a minimum value $\Delta f_{\min}$, then the RES converter stores the MPP power, to be called $P_{\mathrm{mpp},fr}$, and continuously reduces the power generated up to frequency deviation $\Delta f_{\max}$, where the power is zero. The value of $\Delta f_{\min}$ should be higher than M_P in order to prevent interaction with the battery inverter droop and limiting the power when not required. Since the value of $P_{\mathrm{mpp},fr}$ is taken instead of the rated power S_{pv}, the RES power starts to be reduced just when $\Delta f_m > \Delta f_{\min}$, resulting in a faster control. The frequency sensing and filtering H_f, and the relationship between the frequency deviation and the reference RES power P^*_{RES} are shown in Fig. 5.

The implementation of the RES power regulation is described here for a PV system, as well as for a wind-energy conversion system. The PV generator and two-stage PV inverter are shown in Fig. 6(a), while the small WT, the permanent magnet synchronous generator, and the ac/dc stage of the wind-energy ac/ac converter are shown in Fig. 6(b). In order to carry out the PV power reduction, the first stage of the PV inverter, which is a dc/dc boost converter, is controlled as shown in Fig. 7. When Δf_m exceeds $\Delta f_{\min}$, then the MPPT algorithm is cancelled and the PV voltage reference is frozen to its last value $v_{\mathrm{pv,mpp},fr}$. The PV voltage is regulated by means of a PI controller [9]. On the other hand, power reference P^*_{pv} is divided by the measured PV voltage $v_{\mathrm{pv},m}$. Then, the lowest value is selected as the current reference for the inner current control. In so doing, when $\Delta f_m > \Delta f_{\min}$, the power regulation is active, with $v_{\mathrm{pv}} > v_{\mathrm{pv,mpp}}$. However, there are situations in which the power reference can no longer be delivered, for example, after an irradiance drop. In these cases, the PV voltage decreases and the control switches to voltage regulation, which prevents

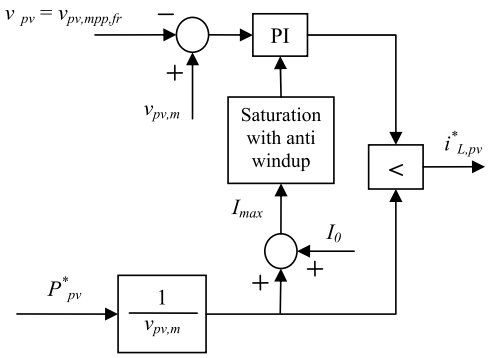

Fig. 7. PV power regulation of the PV boost converter.

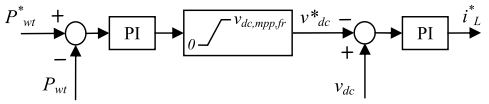

Fig. 8. WT power regulation of the WT boost converter.

a PV voltage drop in the system. The voltage control is maintained until Δf_m decreases to below $\Delta f_{\min}$ and the MPPT is then performed. More details about this technique are shown in [26].

In order to carry out the power reduction in a small WT system, the WT boost converter is controlled as shown in Fig. 8. When Δf_m exceeds $\Delta f_{\min}$, then the loop shown in the figure is activated instead of the MPPT algorithm, and the WT voltage reference upper limit is set to the last $v_{\rm dc}$ value, $v_{\rm dc,mpp,fr}$. In order to reduce the power, the first PI controller reduces the voltage reference, which in turn causes the inductor current to increase. As a result, the voltage and, consequently, the turbine speed are reduced. The system thus evolves toward the low-speed region of the $P-\omega$ curve, which makes it possible to reduce the power ensuring at the same time a safe turbine speed. However, there are situations in which the power reference can no longer be delivered, for example, after a wind speed drop. In these cases, the WT voltage increases until it is limited to $v_{\rm dc,mpp,fr}$, which prevents from overspeeding the generator. The voltage control is maintained until Δf_m decreases to below $\Delta f_{\min}$ and the MPPT is then performed. More details about this technique can be consulted in [27], where a similar control is applied.

One benefit of the power curtailment presented for the RES systems is that only the dc/dc converter control is modified. On the contrary, the RES inverter basic control remains unchanged, regulating the bus voltage and grid current during power limitation too. However, due to the continuous frequency variation caused by the proposed method, occurring not only during power limitation but also during MPPT, some modifications of certain inverter functionalities are required. Although an in-depth analysis is out of the scope of this paper, a brief discussion about grid synchronization and islanding detection is carried out here.

During operation, the voltage frequency evolves according to (3), where δf is obtained as shown in Fig. 4. Because the term δf is related to the battery energy management, its variation is slow with regard to the term $M_P \cdot p$. For this reason, the frequency variation caused by the proposed method implies the same synchronization requirement as for the conventional droop method. For the conventional droop method, the frequency variation can be very fast in the event of load connections/disconnections, and high-performance PLL methods are required [28]–[31]. In any case, errors in the frequency estimation during load transients occur. This will cause reactive power injection by the RES inverter, which will be compensated by the battery inverters.

In stand-alone systems in which security risks could arise, islanding detection can be an important issue. Concerning islanding detection methods, it is well known that, in grid-connected inverters, frequency-shift methods are generally preferred overvoltage shift or impedance measurement methods. This is mainly due to both its lower grid perturbation and its success in islanding detection [32], [33]. Frequency-shift methods could also be applied to stand-alone systems, provided that the frequency limits are expanded beyond $f_0 \pm \Delta f_{\max}$. A higher run-on time could also be allowed in comparison with grid-connected systems. The main drawback is that frequency-shift methods could also perturb the grid generation in droop-based stand-alone microgrids. Consequently, further investigation is required in this field concerning either modifications on conventional frequency-shift methods or using other methods that could be more suitable for this type of systems.

D. Noncritical Load Operation

If the system has noncritical loads which can be regulated, their power can be controlled as a function of the grid frequency. Similarly to the RES inverters (see Fig. 5), a $P-f$ curve can also be programmed so that the consumed power is reduced when the frequency is low. The frequency deviation limits can be set independently of the RES regulation but, in this paper, they will be considered as the opposite of the RES regulation limits, that is, $-\Delta f_{\min}$ and $-\Delta f_{\max}$. Typical programmable loads include thermal loads such as water heaters, refrigerators, and air conditioning units [34], [35].

If load regulation is not feasible or all noncritical loads have already been disconnected, then the system should be shutdown whenever the frequency is very low in order to prevent irreversible damage to the batteries. The value of the shutdown frequency deviation is defined as $-\Delta f_{\rm stop}$. If load regulation is feasible, then the shutdown frequency deviation should be $\Delta f_{\rm stop} > \Delta f_{\min}$, so that the system does not shutdown when the load regulation is active. However, if the loads do not allow for regulation, it should just be $\Delta f_{\rm stop} > M_P$ in order to prevent interaction with the battery inverter droop.

III. Operating Modes

Depending on the values of δf and Δf, there are five operating modes. These operating modes are defined in Table I, and the transitions from one mode to another are shown in Fig. 9 and explained below for two batteries. Fig. 10 shows the frequency deviation for the different operating modes.

TABLE I
OPERATING MODES

Operating mode	Frequencies Δf, δf_1, and δf_2	Battery voltages and currents $v_{\mathrm{bat}1}$, $v_{\mathrm{bat}2}$, $i_{\mathrm{bat}1}$, and $i_{\mathrm{bat}2}$	PV inverters	Noncritical loads
Mode I: Normal operation	$\delta f = 0$ for both batteries $-\Delta f_{\min} < -M_P < \Delta f < M_P < \Delta f_{\min}$	v_{bat} within limits for both batteries i_{bat} within limits for both batteries	MPPT	As required
Mode II: One battery charged	$\delta f > 0$ for one battery $\delta f = 0$ for the other $-\Delta f_{\min} < -M_P < \Delta f < M_P < \Delta f_{\min}$	$v_{\mathrm{bat}} = v_{\mathrm{bat,max}}$ or $i_{\mathrm{bat}} = -i_{\mathrm{bat},c,\mathrm{max}}$ for one battery v_{bat} and i_{bat} within limits for the other	MPPT	As required
Mode III: PV power limitation	$\delta f > 0$ for both batteries $\Delta f_{\min} < \Delta f < \Delta f_{\max}$	$v_{\mathrm{bat}} = v_{\mathrm{bat,max}}$ or $i_{\mathrm{bat}} = -i_{\mathrm{bat},c,\mathrm{max}}$ for one battery $v_{\mathrm{bat}} = v_{\mathrm{bat,max}}$ or $i_{\mathrm{bat}} = -i_{\mathrm{bat},c,\mathrm{max}}$ for the other	Power limitation	As required
Mode IV: One battery discharged	$\delta f < 0$ for one battery $\delta f = 0$ for the other $-\Delta f_{\min} < -M_P < \Delta f < M_P < \Delta f_{\min}$	$v_{\mathrm{bat}} = v_{\mathrm{bat,min}}$ or $i_{\mathrm{bat}} = i_{\mathrm{bat},d,\mathrm{max}}$ for one battery v_{bat} and i_{bat} within limits for the other	MPPT	As required
Mode V: Load regulation	$\delta f < 0$ for both batteries $-\Delta f_{\max} < \Delta f < -\Delta f_{\min}$	$v_{\mathrm{bat}} = v_{\mathrm{bat,min}}$ or $i_{\mathrm{bat}} = i_{\mathrm{bat},d,\mathrm{max}}$ for one battery $v_{\mathrm{bat}} = v_{\mathrm{bat,min}}$ or $i_{\mathrm{bat}} = i_{\mathrm{bat},d,\mathrm{max}}$ for the other	MPPT	Load regulation

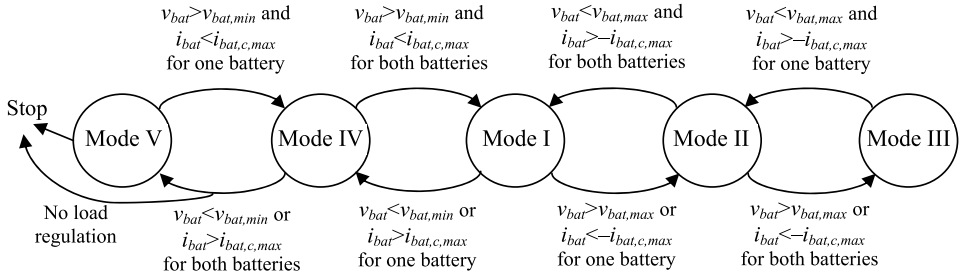

Fig. 9. Transitions between operating modes.

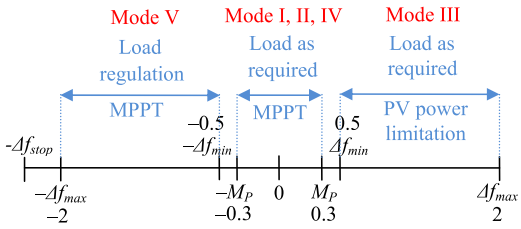

Fig. 10. Frequency deviation (Hz) and operating modes.

A. Mode I: Normal Operation

In Mode I, the battery voltages and currents are within limits, and as a result, from Fig. 4, $\delta f = 0$ for both batteries. By means of (1) and (2), the per-unit power is the same for both batteries, which either absorb or supply the difference between generation and consumption, and their SOCs vary accordingly. Since $\delta f = 0$ from (1), the frequency deviation Δf is between $\pm M_P$. Since it was imposed that $\Delta f_{\min} > M_P$, the PV inverters operate under MPPT and the loads are not regulated (see Fig. 5).

When the voltage for one battery exceeds $v_{\mathrm{bat,max}}$ ($v_{\mathrm{bat}} > v_{\mathrm{bat,max}}$) or the charging current exceeds $i_{\mathrm{bat},c,\mathrm{max}}$($i_{\mathrm{bat}} < -i_{\mathrm{bat},c,\mathrm{max}}$), then the control increases δf, the power absorbed by that battery is reduced and the system switches to Mode II.

On the contrary, if the voltage for one battery decreases to below $v_{\mathrm{bat,min}}$ ($v_{\mathrm{bat}} < v_{\mathrm{bat,min}}$) or the discharging current exceeds $i_{\mathrm{bat},d,\mathrm{max}}$($i_{\mathrm{bat}} > i_{\mathrm{bat},d,\mathrm{max}}$), then the control decreases δf, the power delivered by that battery is reduced and the system switches to Mode IV.

B. Mode II: One Battery Charged

In Mode II, one battery voltage or current is controlled to its maximum value, $v_{\mathrm{bat}} = v_{\mathrm{bat,max}}$ or $i_{\mathrm{bat}} = -i_{\mathrm{bat},c,\mathrm{max}}$, while the other battery voltage and current are within limits. Due to the control, $\delta f = 0$ for the second battery, and $\delta f > 0$ for the first one. As a result, from (4), the second battery is absorbing a higher power than the first battery. Also in this case, since $\delta f = 0$ for one battery inverter, the frequency deviation Δf is between $\pm M_P$ and the net power is not modified.

In this mode, one battery has its voltage and current within limits, and with $\delta f = 0$. If the voltage or current of this battery also exceeds its maximum value, then the net power cannot be absorbed by the whole storage system. In this situation, the power cannot be reorganized between the batteries, as it is carried out for Mode II. According to the control, both batteries increase δf. At first, this has no effect on the net power. However, when the grid frequency deviation becomes higher than $\Delta f_{\min}$, then the PV power starts to be limited and the system switches to Mode III.

On the other hand, in Mode II, there is a battery whose voltage or current is being regulated to its maximum value. When this voltage or current decreases, the battery inverter reduces δf, and the system switches to Mode I.

TABLE II
SYSTEM FEATURES

PV inverter 1 rated power $S_{\mathrm{pv},1}$	5 kVA
PV inverter 2 rated power $S_{\mathrm{pv},2}$	5 kVA
Battery inverter 1 rated power $S_{\mathrm{bat},1}$	6 kVA
Battery inverter 1 output inductance L_1	3 mH
Battery 1 rated capacity C_1	48 kWh
Battery 1 rated voltage $V_{\mathrm{rat},1}$	240 V
Battery 1 absorption voltage $V_{\mathrm{abs},1}$	284 V
Battery inverter 2 rated power $S_{\mathrm{bat},2}$	3 kVA
Battery inverter 2 output inductance L_2	4 mH
Battery 2 rated capacity C_2	18 kWh
Battery 2 rated voltage $V_{\mathrm{rat},2}$	120 V
Battery 2 absorption voltage $V_{\mathrm{abs},2}$	142 V
RMS amplitude of the inverter output voltage E	230 V
RMS amplitude of the ac-bus voltage V	230 V
Droop coefficient M_P	0.3 Hz
Time constant of the real power filter τ_P	10.6 ms
Time constant of the grid frequency filter τ_f	1 s
Minimum frequency deviation Δf_{min}	0.5 Hz
Maximum frequency deviation Δf_{max}	2 Hz

C. Mode III: PV Power Limitation

In Mode III, the voltage or current of all batteries is regulated to its maximum value, $v_{\mathrm{bat}} = v_{\mathrm{bat,max}}$ or $i_{\mathrm{bat}} = -i_{\mathrm{bat},c,\mathrm{max}}$. The control sets $\delta f > 0$ for both batteries, leading to a frequency deviation $\Delta f > \Delta f_{\mathrm{min}}$. As a result, the PV power is reduced according to Fig. 5. This operating point requires a certain net power, which is obtained thanks to the frequency imposed by the control.

In this mode, if the net power increases (for example, due to an irradiance drop), and the system is not able to maintain the voltage or current reference for one battery, then the regulation reduces the frequency deviation to below Δf_{min}, and the system switches to Mode II.

A number of simulations were carried out in order to validate the strategy. An accurate model of the system shown in Fig. 2, comprising two-PV inverters, two-battery inverters, and a number of resistive loads, was developed using the PSIM software. The features of the system are shown in Table II. The first simulation addresses the voltage regulation during the transition from Mode I–Mode II–Mode III–Mode I. This is shown in Fig. 11 and represents the voltage of battery 1 divided by two, the voltage of battery 2, the maximum voltage for both batteries [see Fig. 11(a)], the total PV power, the battery powers [see Fig. 11(b)], the frequency imposed by the battery inverters, and the frequency measured by the PV inverters [see Fig. 11(c)]. During the simulation, the MPP power was always 6 kW, and a number of resistive loads were disconnected and connected.

At the start, the load consumed 4 kW and the net power was therefore $P_T = -2$ kW. Given the fact that the battery voltages were lower than the absorption values, $\delta f = 0$ for both batteries (see Fig. 4), and the system was in Mode I, the per-unit power was the same for both batteries ($P_1 = 2 \cdot P_2$) and the grid frequency was below $f_0 + \Delta f_{\mathrm{min}} = 50.5$ Hz.

Then, at 5 s, a 2.7-kW load was disconnected, leading to a net power $P_T = -4.7$ kW. The battery 2 voltage exceeded its maximum value and, thus, $\delta f_2 > 0$. According to (4), the absorbed power then passed from battery 2 to battery 1, so

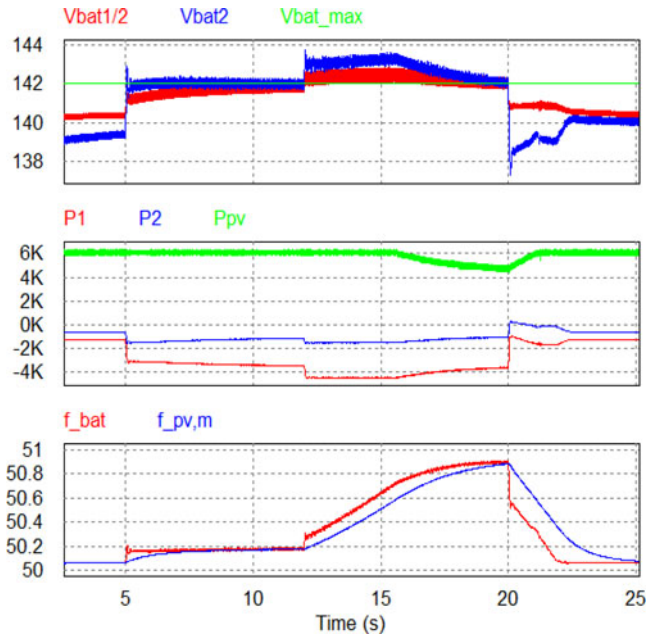

Fig. 11. Voltage regulation during the transition Mode I–Mode II–Mode III–Mode I.

that the battery 2 voltage was controlled, making the system operate in Mode II. Since $\delta f_1 = 0$, the frequency was also lower than $f_0 + \Delta f_{\mathrm{min}}$ in this case, and the PV power required no limitation.

Then, at 12 s, a 1.3-kW load was disconnected, resulting in a net power $P_T = -6$ kW. The voltage of both batteries exceeded their absorption values, meaning that the storage system could not absorb this power and the PV power should be reduced. Thanks to the control, δf_1, δf_2 and the grid frequency increased. Then, when the frequency measured by the PV inverters exceeded $f_0 + \Delta f_{\mathrm{min}} = 50.5$ Hz, the PV power was limited so that both battery voltages were regulated. The system was thus operating in Mode III, with $P_{\mathrm{pv}} = 4.5$ kW and $f = 50.87$ Hz.

Finally, at 20 s, a 4-kW load was connected, leading to a net power $P_T = -0.5$ kW. As a result, battery voltages decreased to below their maximum values, and δf_1 and δf_2 decreased to reach $\delta f_1 = \delta f_2 = 0$. The grid frequency also decreased, the PV inverters performed MPPT, and the system switched to Mode I.

D. Mode IV: One Battery Discharged

In Mode IV, one battery voltage or current is controlled to the reference value, $v_{\mathrm{bat}} = v_{\mathrm{bat,min}}$ or $i_{\mathrm{bat}} = i_{\mathrm{bat},d,\mathrm{max}}$, while the other battery voltage and current are within limits. The control imposes $\delta f < 0$ for the first battery and $\delta f = 0$ for the second one. From (4), the first battery is therefore supplying less power than the second one. Since $\delta f = 0$ for one battery inverter, the frequency deviation Δf is between $\pm M_P$, and the net power is not modified.

In this mode, one battery has its voltage and current within limits, and with $\delta f = 0$. When, for this battery, the voltage drops to below $v_{\mathrm{bat,min}}$ or the discharging current exceeds $i_{\mathrm{bat},d,\mathrm{max}}$, the net power cannot be delivered by the whole storage system.

In this case, the power cannot be reorganized between the batteries, as was the case for Mode IV. According to the control, both batteries reduce δf. At first, this has no effect on the net power. However, when the grid frequency deviation becomes lower than $-\Delta f_{\min}$, the load power starts to be regulated and the system switches to Mode V. If the system does not allow for noncritical load regulation, then the frequency will continue to decrease until $\Delta f < -\Delta f_{\text{stop}}$, where the system shuts down in order to prevent irreversible damage to the batteries.

On the other hand, in Mode IV, there is a battery whose voltage or current is being regulated to its reference value, $v_{\text{bat}} = v_{\text{bat,min}}$ or $i_{\text{bat}} = i_{\text{bat},d,\max}$. When this voltage increases or this current decreases, the battery inverter raises δf, and the system changes to Mode I.

E. Mode V: Load Regulation

In Mode V, the voltage or current of all batteries is regulated to its reference value, $v_{\text{bat}} = v_{\text{bat,min}}$ or $i_{\text{bat}} = i_{\text{bat},d,\max}$. Due to the control, $\delta f < 0$ for both batteries, which results in a frequency deviation $\Delta f < -\Delta f_{\min}$. As a result, the load power is regulated, making it possible to impose the required net power so that the voltage or current is maintained to its reference value.

In this mode, if the net power to be supplied decreases (for example, due to an increase in irradiance), then the regulation increases the frequency deviation to over $-\Delta f_{\min}$, and the system switches to Mode IV.

On the other hand, if all noncritical loads have already been disconnected and the storage system cannot supply the required net power, then $v_{\text{bat}} < v_{\text{bat,min}}$ or $i_{\text{bat}} > i_{\text{bat},d,\max}$ for both batteries, and the control continues to decrease δf until $\Delta f < -\Delta f_{\text{stop}}$, where the system is shutdown in order to prevent irreversible damage to the batteries.

Another simulation is carried out here for the system presented above in Fig. 2 and Table II. It addresses current regulation during the transition from Mode I–Mode IV–Mode V–Mode I. The simulation results are plotted in Fig. 12 and show the battery currents, the maximum discharging current for both batteries [see Fig. 12(a)], the load power, the battery powers [see Fig. 12(b)], the frequency imposed by the battery inverters, and the frequency measured by the controllable load [see Fig. 12(c)]. It was assumed that, due to adverse conditions, both batteries were very hot. In order to protect the batteries, their maximum current was reduced to $i_{\text{bat},d,\max 1} = 20$ A and $i_{\text{bat},d,\max 2} = 10$ A. During the simulation, the PV power was always 0, and a number of resistive loads were disconnected and connected, including a 2.7-kW controllable load.

At the beginning, a 3-kW load was connected to the grid. Since the battery currents were under their maximum values, $\delta f = 0$ for both batteries (see Fig. 4), and the system was in Mode I. As a result, the per-unit power was the same for both batteries ($P_1 = 2 \cdot P_2$), and the grid frequency was higher than $f_0 - \Delta f_{\min} = 49.5$ Hz.

Then, at 5 s, a 2-kW load was connected. The battery 2 current became higher than the maximum value, which led to $\delta f_2 < 0$. The delivered power then passed from battery 2 to battery 1 so that the battery 2 current was controlled, making

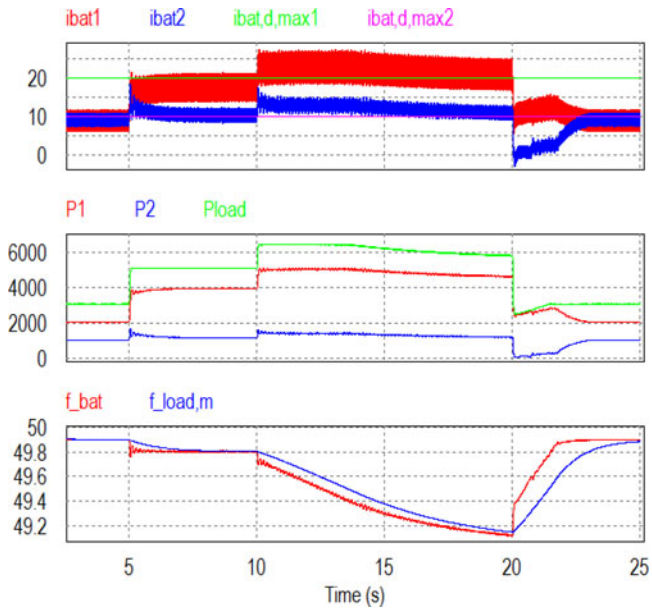

Fig. 12. Current regulation during the transition Mode I–Mode IV–Mode V–Mode I.

the system operate at Mode IV. Since $\delta f_1 = 0$, the frequency was also higher than $f_0 - \Delta f_{\min}$ in this case, and the load did not require regulation.

Next, at 10 s, a 1.4-kW load was connected. At that moment, the currents of both batteries exceeded their maximum values, meaning that the storage system could not deliver the power required and the load needed to be reduced. Thanks to the control, δf_1, δf_2, and the grid frequency decreased. When the frequency measured by the controllable load dropped to below $f_0 - \Delta f_{\min} = 49.5$ Hz, the load power was regulated in such a way that both battery currents were controlled. The system was then operating in Mode V, with $P_{\text{load}} = 5.8$ kW, $P_{\text{load,cont}} = 2.1$ kW, and $f = 49.15$ Hz.

Finally, at 20 s, a 3.4-kW load was disconnected. This caused the battery currents to drop to below their maximum values, and δf_1 and δf_2 increased to reach $\delta f_1 = \delta f_2 = 0$. The grid frequency also increased, the controllable load consumed more power and the system switched to Mode I.

IV. Small-Signal Modeling

Small-signal modeling is used in this paper in order to design the controllers so that a certain stability margin and dynamic response is obtained for the system. In Section IV-A, the small-signal modeling is applied to a system operating in Mode III. Furthermore, it is assumed that there are two batteries and two-battery inverters with identical characteristics. The small-signal modeling for other modes is explained in Section IV-B. Then, the modeling for different battery systems is developed in Section IV-C. The modeling for more than two batteries is not shown in this paper for reasons of space, however it can be readily obtained from the two-battery model.

A. Mode III: Identical Battery System

When both battery systems are identical, the power response can be decoupled into the power distribution response and the net power regulation, as it will be shown in this section. The power distribution is related to the difference between the power supplied by both batteries, $P_1 - P_2$, and will be called difference (D) response. The net power regulation is related to PV and load power regulation, i.e., to the sum of the battery powers, $P_1 + P_2$, and will be called sum (S) response.

The power delivered by a battery inverter to the ac bus can be expressed as [36]

$$P = \frac{V \cdot E}{X} \cdot \sin \delta \tag{7}$$

where *E* is the RMS amplitude of the inverter output voltage, δ is the power angle, *V* is the RMS amplitude of the ac-bus voltage, and *X* is the output reactance. This equation is valid when the output impedance is mainly inductive, whereas in low-voltage grids the line impedance is mainly resistive. However, in this paper, an RMS voltage regulation is carried out instead of an instantaneous voltage regulation [4], [37]. In doing so, the filter inductance also becomes part of the output impedance for the droop method. Given the high value of this filter impedance (the per-unit value is generally about 10%), it is possible to neglect the line impedance for typical low-voltage grids with short lines. However, the analysis presented here is not valid for low-voltage grids with long lines, and a modification of the small-signal modeling should be carried out to account for the line impedance.

In practical applications, δ is very low. Furthermore, the influence of small variations in *E* and *V* on the real power can be disregarded. Applying these approximations and the small-signal analysis to (7), the following is obtained:

$$\hat{P} = \frac{V_0 \cdot E_0}{X} \cdot \hat{\delta} \tag{8}$$

where $V_0 = E_0$ is the rated voltage.

With regard to the difference response, the battery power difference can be readily calculated using (8) as

$$\hat{P}_1 - \hat{P}_2 = \frac{V_0 \cdot E_0}{X} \cdot (\hat{\delta}_1 - \hat{\delta}_2). \tag{9}$$

The difference between the power angles only changes if the frequencies imposed by the battery inverters, f_1 and f_2, are different. By means of the relationship between the power angle and the frequency, and (9), the following applies:

$$\hat{P}_1 - \hat{P}_2 = D_{\mathrm{PL}} \cdot (\hat{f}_1 - \hat{f}_2) \tag{10}$$

$$D_{\mathrm{PL}} = \frac{V_0 \cdot E_0}{X} \cdot \frac{2\pi}{s}. \tag{11}$$

Equation (10) shows that the power distribution can be controlled by changing the frequency difference between the battery inverters, as performed for the conventional droop method.

Concerning the sum response, the sum of P_1 and P_2 can be easily obtained from the power balance as

$$\hat{P}_1 + \hat{P}_2 = \hat{P}_T = \hat{P}_L - \hat{P}_{\mathrm{RES}} \tag{12}$$

where P_{RES} is the total renewable-energy-source power, and P_L is the total load power.

The total load can include linear loads and constant power loads (CPLs). While the real power of the CPLs does not depend on the grid voltage, the real power of the linear loads increases as the voltage augments. However, this has a small effect on the power response in this case, since the load impedance is always much higher than the inverter output impedance [38], [39]. Furthermore, the influence on the real power is much smaller than on the reactive power due to the lower sensitivity to voltage variations [40]. The power P_L is also independent of the frequency in Mode III and will not therefore be considered for the analysis.

The PV and wind-energy systems can be considered as constant power sources (CPSs) since their power depends on the resource during MPPT operation and on the power reference during power limitation [41]. As a result, the real power of the RES is independent of the grid voltage. However, the power P_{RES} does depend on the frequency according to Fig. 5, which leads to the following expression:

$$P_{\mathrm{RES}} = \frac{\Delta f_{\max} - \Delta f_m}{\Delta f_{\max} - \Delta f_{\min}} \cdot P_{\mathrm{mpp},t} \tag{13}$$

where $P_{\mathrm{mpp},t}$ is the total stored MPP power.

Applying small-signal analysis to (13) and taking account of the first-order filter H_f shown in Fig. 5, gives

$$\hat{P}_{\mathrm{RES}} = -\frac{P_{\mathrm{mpp},t}}{\Delta f_{\max} - \Delta f_{\min}} \cdot H_f \cdot \Delta \hat{f}. \tag{14}$$

It can be considered that the grid frequency deviation Δf is the average between the frequency deviations imposed by both inverters. As a result, from (12) and (14)

$$\hat{P}_1 + \hat{P}_2 = S_{\mathrm{RES}}(\hat{f}_1 + \hat{f}_2) \tag{15}$$

$$S_{\mathrm{RES}} = \frac{1}{2} \cdot \frac{P_{\mathrm{mpp},t}}{\Delta f_{\max} - \Delta f_{\min}} \cdot H_f. \tag{16}$$

Equation (15) shows that the net power can be regulated by changing the sum of battery inverters frequencies, in effect thanks to the PV power regulation shown in Fig. 5.

Equations (10) and (15) represent the power response of the system to frequency variations. Once the system plant has been obtained, the control model can now be developed. The frequency of the battery inverters is imposed as dictated by (3), where the first part of the equation represents the conventional droop method and the term δf is added according to Fig. 4. Since the analysis is based on Mode III, $\delta f_d = 0$ and $\delta f = \delta f_c$. It is also assumed that the battery voltages are being regulated, which leads to $\delta f = \delta f_{c,v}$ (see Fig. 4). The modeling of the current regulation is not shown in this paper because it is similar and simpler than the modeling of the voltage regulation. Taking these considerations into account, (3) and Fig. 4, the following is obtained:

$$f = f_0 - \frac{M_P}{S_{\mathrm{bat}}} \cdot H_P \cdot P + C_{c,v} \cdot S_v \cdot (v_{\mathrm{bat}} - v_{\mathrm{bat,max}}) \tag{17}$$

where H_P models the measurement and sampling of the power, and S_v models the sampling of the battery voltage.

Applying small-signal analysis to (17) gives

$$\hat{f} = -\frac{M_P}{S_{\text{bat}}} \cdot H_P \cdot \hat{P} + C_{c,v} \cdot S_v \cdot \hat{v}_{\text{bat}}. \tag{18}$$

Considering the small-signal analysis of the Thevenin lead-acid battery equivalent circuit model, the battery power to voltage transfer function G_{bat} can be obtained as [42]

$$\frac{\hat{v}_{\text{bat}}}{\hat{p}_{\text{bat}}} = -\frac{C\ R_C R_S \cdot s + R_C + R_S}{C\ R_C(V_{\text{bat}} + R_S I_{\text{bat}})s + V_{\text{bat}} + (R_C + R_S)I_{\text{bat}}} \tag{19}$$

where p_{bat} is the power delivered by the battery, V_{bat} and I_{bat} are the battery voltage and current (dc operating points), R_S is the internal resistance, and R_C and C represent the first-order dynamics of the battery. Parameters R_S, R_C, and C can be considered constant for modeling purposes since the SOC changes, but slightly within the operating range of the voltage regulation.

Due to the dc-bus capacitor voltage regulation, the power delivered by the battery inverter P is delayed in relation to p_{bat}. A first-order filter, named B, will be used to model this delay. In this case, it also can be considered that $(R_C + R_S) \cdot I_{\text{bat}} \ll V_{\text{bat}}$. Based on these two considerations, (19) leads to the following:

$$\begin{aligned} \hat{v}_{\text{bat}} &= -\frac{1}{V_{\text{bat}}} \cdot \frac{C\ R_C R_S \cdot s + R_C + R_S}{C\ R_C s + 1} \cdot B \cdot \hat{P} \\ &= -G_{\text{bat}} \cdot B \cdot \hat{P}. \end{aligned} \tag{20}$$

From (18) and (20), the frequency reference can be obtained as a function of P

$$\hat{f} = -(D_{\text{CON}} + S_{\text{BAT}}) \cdot \hat{P} \tag{21}$$

$$D_{\text{CON}} = \frac{M_P}{S_{\text{bat}}} \cdot H_P \tag{22}$$

$$S_{\text{BAT}} = C_{c,v} \cdot S_v \cdot G_{\text{bat}} \cdot B. \tag{23}$$

Equation (21) represents how the control of each battery inverter changes its frequency when its delivered power varies. By means of (10), and (21) applied to both inverters, the characteristic equation for the power distribution, den_D, can be obtained as

$$den_D = 1 + D_{\text{PL}}(D_{\text{CON}} + S_{\text{BAT}}). \tag{24}$$

The conventional droop control, represented by D_{CON}, was initially designed to have an effect on the power distribution [43], while the voltage regulation, represented by S_{BAT}, was initially designed to have an effect on the net power [18]. However, as (24) shows, both terms are important for the power distribution response. To evaluate the influence of each term more precisely, the root locus diagrams of den_D for different values of M_P and K_P are shown in Fig. 13, where K_P is the proportional parameter of PI controller $C_{c,v}$. The analysis is carried out for the system presented in Table II but assuming that the features of battery inverter 2 are those of battery inverter 1, in other words identical battery systems. As can be observed in Fig. 13, the characteristic equation den_D has four important roots. Poles

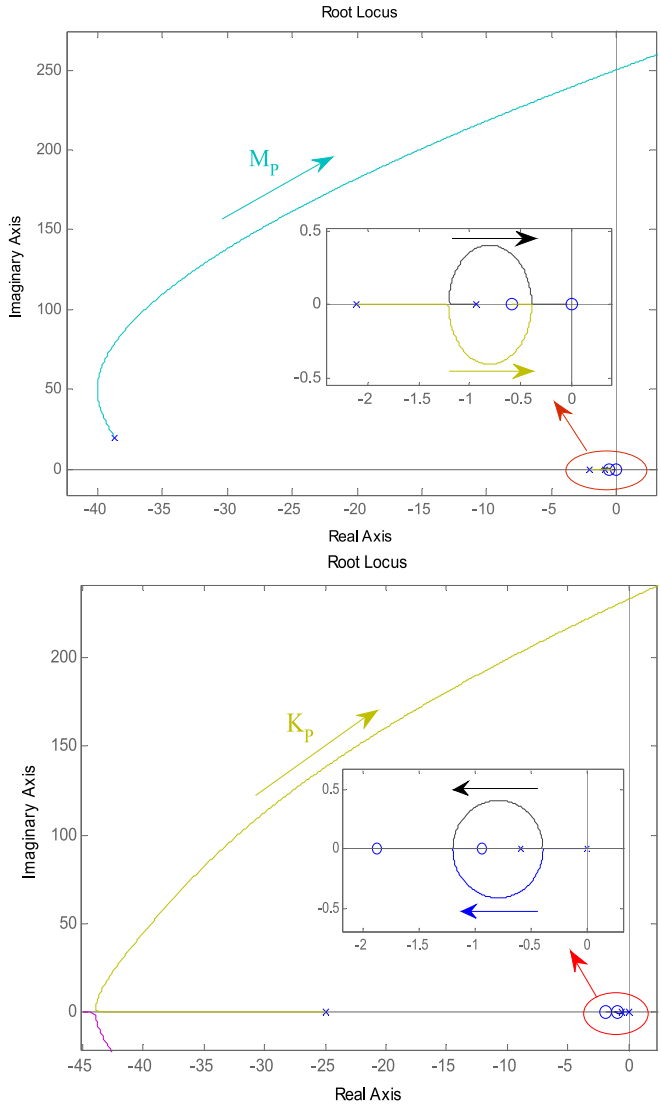

Fig. 13. Root locus diagrams for den_D. (a) M_P increasing ($K_P = 0.07$). (b) K_P increasing ($M_P = 0.3$ Hz).

λ_1 and λ_2, the two poles closest to the origin, are the dominant ones. The rapidity of the power distribution response is therefore determined by them. The appearance of these slow poles is due to the battery voltage regulation (term δf or transfer function S_{BAT}), since they are not present for the conventional droop control [43]. On the other hand, poles λ_3 and λ_4, the two poles farthest away from the origin, represent the stability margin of the power distribution response. Although these poles are also influenced by the voltage regulation, their appearance is due to the conventional droop method (term $M_P \cdot p$ or transfer function D_{CON}). As can be observed in Fig. 13(a), increasing M_P moves poles λ_3 and λ_4 closer to the imaginary axis, making the system less damped, while at the same time reduces the real part of λ_1 and λ_2, slowing down the response. On the other hand, as shown in Fig. 13(b), increasing K_P has the same effect on λ_3 and λ_4, making the response less damped, but increases the real part of λ_1 and λ_2, speeding up the response.

By means of (15), and (21) applied to both inverters, the characteristic equation for the net power, den_S, can be obtained

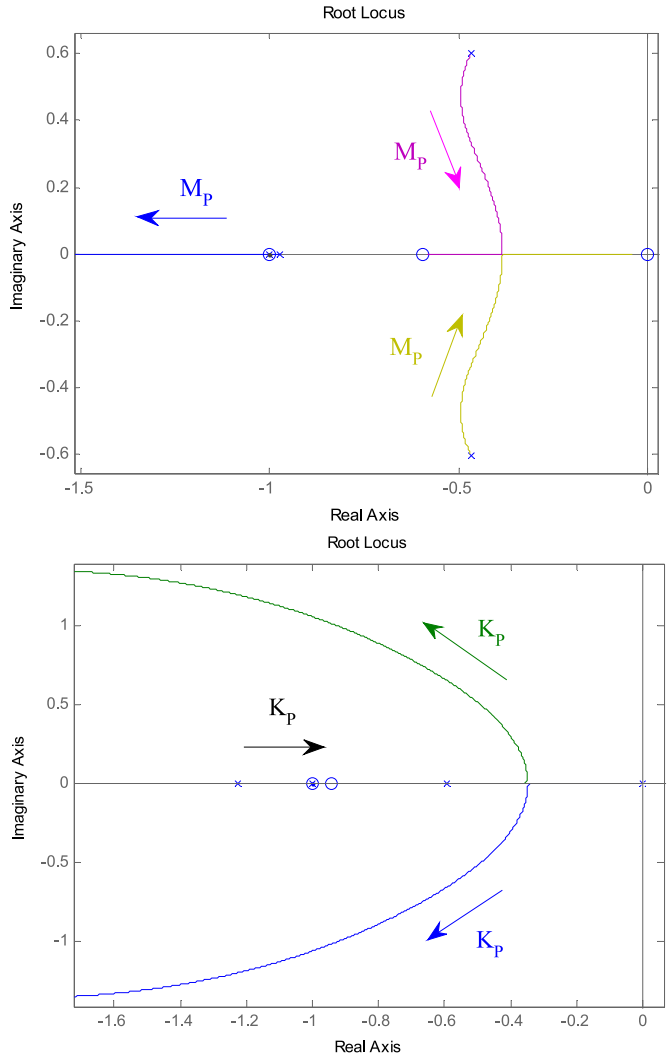

Fig. 14. Root locus diagrams for den_S. (a) M_P increasing ($K_P = 0.07$). (b) K_P increasing ($M_P = 0.3$ Hz).

as

$$den_S = 1 + S_{\mathrm{RES}}(D_{\mathrm{CON}} + S_{\mathrm{BAT}}). \tag{25}$$

This expression shows that, also in this case, both terms D_{CON} (due to $M_P \cdot p$) and S_{BAT} (due to δf) are important for the net power response. The influence of each term on den_S is also evaluated here by means of the root locus analysis. The root locus diagrams of den_S for different values of M_P and K_P are shown in Fig. 14 for the system above. As can be observed in the figures, den_S has three important roots. Poles λ_1 and λ_2 are the ones closest to the origin, and their appearance is due to the battery voltage regulation (term δf or transfer function S_{BAT}). On the other hand, pole λ_3 is the one farthest away from the origin and its appearance is due to the conventional droop method (term $M_P \cdot p$ or transfer function D_{CON}), since it does not exist when the droop control is not present [18]. As shown in Fig. 14(a), increasing M_P moves λ_1 and λ_2 closer to the real axis, making the response more damped. The response also becomes slower if M_P is high enough. On the other hand, as also shown in Fig. 14(b), increasing K_P slightly changes the damping of λ_1 and λ_2 (from a certain value of K_P) and has little effect on the pole λ_3. Furthermore, if K_P is high enough, the real pole λ_3, which is more affected by M_P, becomes dominant.

Although the demonstration is not shown here for reasons of space, the characteristic equations den_D and den_S are exactly the same for an *n* identical battery system if a slight modification is made, the 2 in A_{RES} expression (see (16)) must be changed by *n*. As a result, the analysis carried out in this section is also applicable to an n identical battery system.

B. Other Modes: Identical Battery System

The system modeling when operating in Modes I, II, IV, and V can be obtained from the analysis developed in Section IV-A for Mode III. In this section, the differences in relation to Mode III are highlighted for the other operating modes.

When the system is operating in Mode V, (24) and (25) apply for the power distribution and net power responses, respectively. However, the total controllable load power must be considered in S_{RES} instead of the total MPP power $P_{\mathrm{mpp},t}$ (see (16)), controller $C_{d,v}$ must be considered in S_{BAT} instead of $C_{c,v}$ (see (23)), and the battery model parameters must be given for a low SOC level (see (20)).

When the system is operating in Modes II or IV, the net power is not modified because the RES or load power is not changed by the control. As a result, the net power response does not apply in these modes. With regard to the power distribution response, (24) must be modified. In these modes, only one battery is varying the term δf, while in the other, the controller outputs are inactive due to saturation $\delta f = 0$ (see Fig. 4). As a result, (21) is only valid for one battery inverter, and in the other $S_{\mathrm{BAT}} = 0$. On account of this, the characteristic equation for the power distribution now becomes

$$den_D = 1 + D_{\mathrm{PL}}(D_{\mathrm{CON}} + S_{\mathrm{BAT}}/2). \tag{26}$$

Furthermore, controller $C_{c,v}$ and a high-SOC-battery model must be used in Mode II, while controller $C_{d,v}$ and a low-SOC-battery model must be used in Mode IV. Equation (26) can be analyzed by means of the root locus diagram for den_D of Fig. 13, considering K_P is equal to half the K_P value used in Mode III. As a result, the power distribution response for Modes II and IV is more damped and slower than for Mode III.

Finally, when the system is operating in Mode I, both battery voltage controllers are inactive because their outputs are saturated to $\delta f = 0$ (see Fig. 4). As a result, only the conventional droop method applies, which leads to

$$den_D = 1 + D_{\mathrm{PL}} \cdot D_{\mathrm{CON}}. \tag{27}$$

In this case, poles λ_1 and λ_2 of Fig. 13 do not appear, and the power distribution response therefore becomes much quicker and more damped, as can be observed in Fig. 13 for $K_P = 0$ and in [43].

C. Different Battery System

If the two-battery systems are not identical, even if they have the same per-unit characteristics, then the power response cannot be decoupled. For Mode III, proceeding similarly to

Section IV-A, the characteristic equation for the power response, den_{DS}, is expressed as

$$\begin{aligned} den_{DS} = {} & 1 + 1/2\cdot(D_{\mathrm{PL}} + S_{\mathrm{RES1}})(D_{\mathrm{CON1}} + S_{\mathrm{BAT1}}) \\ & + 1/2\cdot(D_{\mathrm{PL}} + S_{\mathrm{RES2}})(D_{\mathrm{CON2}} + S_{\mathrm{BAT2}}) \\ & + 1/2\cdot(D_{\mathrm{RES1}} + S_{\mathrm{RES2}})(D_{\mathrm{CON1}} + S_{\mathrm{BAT1}}) \\ & \times(D_{\mathrm{CON2}} + S_{\mathrm{BAT2}}) \end{aligned} \tag{28}$$

$$D_{\mathrm{PL1}} = D_{\mathrm{PL2}} = D_{\mathrm{PL}} = 2\cdot\frac{V\cdot E}{X_1 + X_2}\cdot\frac{2\pi}{s} \tag{29}$$

$$S_{\mathrm{RES1}} = \frac{X_2}{X_1 + X_2}\cdot\frac{P_{\mathrm{mpp},t}}{\Delta f_{\max} - \Delta f_{\min}}\cdot H_f \tag{30}$$

$$S_{\mathrm{RES2}} = \frac{X_1}{X_1 + X_2}\cdot\frac{P_{\mathrm{mpp},t}}{\Delta f_{\max} - \Delta f_{\min}}\cdot H_f \tag{31}$$

$$D_{\mathrm{CON1}} = \frac{M_P}{S_{\mathrm{bat},1}}\cdot H_P, \quad D_{\mathrm{CON2}} = \frac{M_P}{S_{\mathrm{bat},2}}\cdot H_P \tag{32}$$

$$\begin{aligned} S_{\mathrm{BAT1}} &= C_{c,v1}\cdot S_{v1}\cdot G_{\mathrm{bat1}}\cdot B_1, \\ S_{\mathrm{BAT2}} &= C_{c,v2}\cdot S_{v2}\cdot G_{\mathrm{bat2}}\cdot B_2. \end{aligned} \tag{33}$$

The different control parameters of each battery inverter can be designed according to Section IV-A, assuming that all the inverters operating are identical. Equations (28)–(33) then make it possible to verify the real dynamic response. In effect, in doing so, it can be verified that the dynamic response for the different battery system remains similar to the one for the identical battery system (design system).

V. Experimental Results

The proposed frequency-based energy-management strategy was validated by experimental tests. Two batteries with their inverters were connected in parallel and generated the ac grid. A load bank and two-PV emulators with their inverters were connected to the grid. The battery and PV inverters are commercial ones, with a modified configuration, in order to implement the proposed strategy. More precisely, the proposed droop method presented by (3), where δf is obtained from (5) and Fig. 4, was programmed in the battery inverters, while the PV power regulation, represented by Figs. 5 and 7, was programmed in the PV inverters. The system features are shown in Table II, where it can be observed that the two-battery systems have different characteristics. Precision power analyzer WT1800 served to obtain the data, supplying voltages, currents, powers, and frequencies every 50 ms.

The first test was conducted to validate the battery voltage regulation during the transition from Mode I–Mode II–Mode III, similarly to the simulation presented in Fig. 11. The experimental results are shown in Fig. 15 and represent the battery 1 voltage divided by two, the battery 2 voltage, the maximum voltage for both batteries [see Fig. 15(a)], the battery powers, the load power, the total PV power [see Fig. 15(b)], and the grid frequency [see Fig. 15(c)]. At the start, both battery voltages were lower than their maximum values. As a result, the battery inverters shared the power in proportion to their ratings

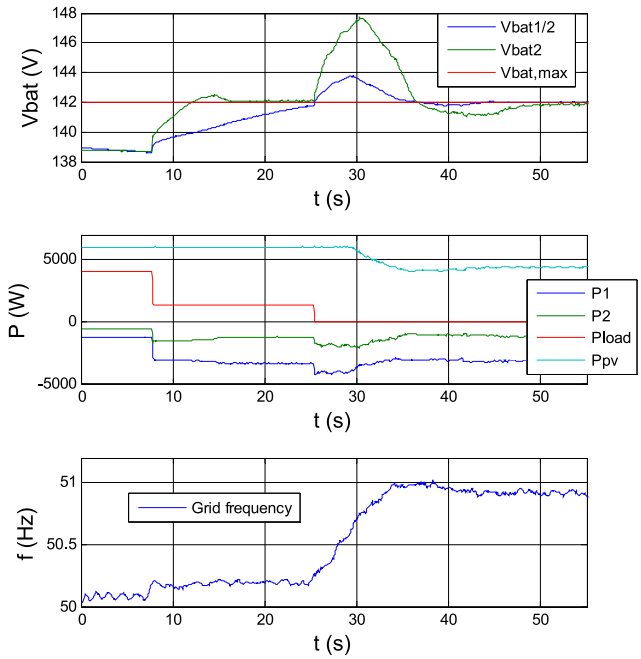

Fig. 15. Voltage regulation during the transition Mode I–Mode II–Mode III.

($P_1 = 2\cdot P_2$), the frequency was close to 50 Hz and the system was operating in Mode I. Then, at about 8 s, a 2.6-kW load was disconnected. The battery 2 voltage exceeded its maximum value but, thanks to the control, the absorbed power switched from battery 2 to battery 1 so that the battery 2 voltage was controlled, making the system operate in Mode II. The grid frequency increased in this mode but remained lower than $f_0 + \Delta f_{\min} = 50.5$ Hz because the PV power did not need to be limited. Then, at about 25 s, a 1.3-kW load was also disconnected, making the voltage of both batteries exceed their maximum value. As a result, the grid frequency was increased by the control. Then, when the frequency measured by the PV inverters became higher than 50.5 Hz, the PV power was reduced so that both battery voltages were regulated, making the system operate in Mode III. The figure shows how the proposed strategy is successful in controlling the absorption voltage of one or two batteries as required, while at the same time making the most of the solar energy, yet with no need for communication cables.

The second test validated the battery current regulation during the transition from Mode I–Mode IV–Stop, in a similar way to the simulation presented in Fig. 12. The experimental results, shown in Fig. 16, represent the battery currents, the maximum discharging current for both batteries [see Fig. 16(a)], the load power, the battery powers [see Fig. 16(b)], and the grid frequency [see Fig. 16(c)]. It was assumed that, due to adverse conditions, both batteries were very hot. In order to protect them, their maximum current was reduced to $i_{\mathrm{bat},d,\max 1} = 20$ A and $i_{\mathrm{bat},d,\max 2} = 10$ A. During the test, the PV power was always 0, and there were no controllable loads. At the beginning, both battery currents were below their maximum values. Hence, the system operated in Mode I, the load power was shared by

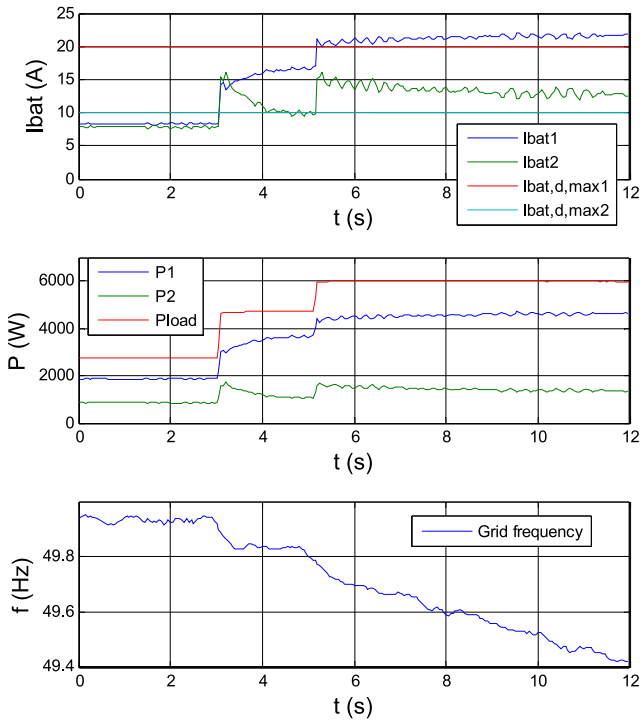

Fig. 16. Current regulation during the transition Mode I–Mode IV–Stop.

the inverters, and the frequency was close to 50 Hz. At about 3 s, a 2-kW load was connected. The battery 2 current then became higher than 10 A, and as a result, the control made battery inverter 1 deliver more power so that the battery 2 current was regulated, making the system operate in Mode II. Then, at about 5 s, a 1.3-kW load was also connected, making each battery current exceed its maximum value. As a result, the grid frequency was reduced by the control. Since there were no controllable loads in this test, the frequency continued decreasing until it reached value $f_0 - \Delta f_{\text{stop}} = 49.4$ Hz, when the system stopped in order to protect the batteries. The figure shows how the proposed strategy manages to either control the current of one battery or to stop the system as required with no need for communication cables. Furthermore, the value of Δf_{stop} can be configured in order to control the overload time, depending on the system thermal properties.

VI. Conclusion

This paper presents a new energy-management strategy for stand-alone systems with distributed energy storage. The energy management is carried out with no need for communication cables between the inverters and to a central supervisor, using frequency as a communication signal, resulting in a more reliable and cost-effective system. During normal operation, the power is shared among the various battery inverters thanks to the conventional droop method. Then, when some batteries are fully charged or are absorbing too much current, the frequency is increased. As a result, the power is first transferred from some of the batteries to the others. However, if all batteries have reached the maximum voltage or current, then the renewable-energy sources detect the high frequency and reduce their power in order to adjust the battery voltages or currents. Similarly, when the batteries are either fully discharged or delivering excessive current, then the frequency is decreased. This makes it possible to regulate the voltage/current of one or more batteries as required. Then, if all batteries reach their minimum voltage or maximum discharging current, the less critical loads are regulated. If this is not possible, then the system stops in order to prevent serious damage to the batteries.

Small-signal modeling for the whole system is carried out. This modeling makes it possible to evaluate the influence of the new control in relation to the conventional droop method, to design the main control parameters even for uncertain systems, and to validate the power response dynamics and stability for a given system.

The proposed strategy is validated by means of simulation and experimental tests for a system with two-battery inverters, two-PV inverters, and a number of loads. The results show how the regulation of battery voltages or currents, the PV power reduction and the noncritical loads control are correctly performed. As a result, the energy management is successfully carried out for the most critical situations with no use of communication cables.

References

[1] D. P. Kaundinya, P. Balachandra, and N. H. Ravindranath, "Grid-connected versus stand-alone energy systems for decentralized power—A review of literature," *Renew. Sustainable Energy Rev.*, vol. 13, pp. 2041–2050, 2009.

[2] K. Bandara, T. Sweet, and J. Ekanayake, "Photovoltaic applications for off-grid electrification using novel multi-level technology with energy storage," *Renew. Energy*, vol. 37, pp. 82–88, 2012.

[3] L. Wang, X. Q. Guo, H. R. Gu, W. T. Wu, and J. M. Guerrero, "Precise modeling based on dynamic phasors for droop-controlled parallel-connected inverters," in *Proc. Int. Symp. Ind. Electron.*, 2012, pp. 475–480.

[4] M. C. Chandorkar, D. M. Divan, and R. Adapa, "Control of parallel connected inverters in standalone ac supply systems," *IEEE Trans. Ind. Appl.*, vol. 29, no. 1, pp. 136–143, Jan./Feb. 1993.

[5] H. Ghoddami, M. B. Delghavi, and A. Yazdani, "An integrated wind-photovoltaic-battery system with reduced power-electronic interface and fast control for grid-tied and off-grid applications," *Renew. Energy*, vol. 45, pp. 128–137, 2012.

[6] K. Strunz, E. Abbasi, and D. N. Huu, "DC microgrids for wind and solar power integration," *IEEE J. Emerg. Sel. Topics Power Electron.*, vol. 2, no. 1, pp. 115–126, Mar. 2014.

[7] F. Valenciaga and P. F. Puleston, "Supervisor control for a stand-alone hybrid generation system using wind and photovoltaic energy," *IEEE Trans. Energy Convers.*, vol. 20, no. 2, pp. 398–405, Jun. 2005.

[8] A. Urtasun, P. Sanchis, I. San Martín, J. López, and L. Marroyo, "Modeling of small wind turbines based on PMSG with diode bridge for sensorless maximum power tracking," *Renew. Energy*, vol. 55, pp. 138–149, 2013.

[9] A. Urtasun, P. Sanchis, and L. Marroyo, "Adaptive voltage control of the dc/dc boost stage in PV converters with small input capacitor," *IEEE Trans. Power Electron.*, vol. 28, no. 11, pp. 5038–5048, Nov. 2013.

[10] E. A. A. Coelho, P. C. Cortizo, and P. F. D. Garcia, "Small-signal stability for parallel-connected inverters in stand-alone AC supply systems," *IEEE Trans. Ind. Appl.*, vol. 38, no. 2, pp. 533–542, Mar./Apr. 2002.

[11] T. W. Li and C. Kao, "An accurate power control strategy for power-electronics-interfaced distributed generation units operating in a low-voltage multibus microgrid," *IEEE Trans. Power Electron.*, vol. 24, no. 12, pp. 2977–2988, Dec. 2009.

[12] A. Mohd, E. Ortjohann, D. Morton, and O. Omari, "Review of control techniques for inverters parallel operation," *Electr. Power Syst. Res.*, vol. 80, pp. 1477–1487, 2010.

[13] D. Wu, J. M. Guerrero, J. C. Vasquez, T. Dragicevic, and F. Tang, "Coordinated power control strategy based on primary-frequency-signaling for islanded microgrids," in *Proc. Energy Convers. Congr. Expo.*, 2013, pp. 1033–1038.
[14] J. M. Guerrero, J. C. Vasquez, J. Matas, L. G. de Vicuña, and M. Castilla, "Hierarchical control of droop-controlled AC and DC microgrids—A general approach toward standardization," *IEEE Trans. Ind. Electron.*, vol. 58, no. 1, pp. 158–172, Jan. 2011.
[15] A. K. Daud and M. S. Ismail, "Design of isolated hybrid systems minimizing costs and pollutant emissions," *Renew. Energy*, vol. 44, pp. 215–224, 2012.
[16] J. Kim, S. Kim, and J. Jeon, "Coordinated state-of-charge control strategy for microgrid during islanded operation," in *Proc. IEEEE 3rd Power Electron. Distrib. Gener. Syst. Symp.*, 2012, pp. 25–28.
[17] D. E. Olivares, C. A. Canizares, and M. Kazerani, "A centralized optimal energy management system for microgrids," in *Proc. Power Energy Soc. Gen. Meet.*, 2011, pp. 24–29.
[18] A. Urtasun, P. Sanchis, D. Barricarte, and L. Marroyo, "Energy management strategy for a battery-diesel stand-alone system with distributed PV generation based on grid frequency modulation," *Renew. Energy*, vol. 66, pp. 325–336, 2014.
[19] E. Serban and H. Serban, "A control strategy for a distributed power generation microgrid application with voltage- and current-controlled source converter," *IEEE Trans. Power Electron.*, vol. 25, no. 12, pp. 2981–2992, Dec. 2010.
[20] H. Kakigano, Y. Miura, and T. Ise, "Distribution voltage control for DC microgrids using fuzzy control and gain-scheduling technique," *IEEE Trans. Power Electron.*, vol. 28, no. 5, pp. 2246–2258, May 2013.
[21] T. Dragicevic, J. M. Guerrero, J. C. Vasquez, and D. Skrlec, "Supervisory control of an adaptive-droop regulated DC microgrid with battery management capability," *IEEE Trans. Power Electron.*, vol. 29, no. 2, pp. 695–706, Feb. 2014.
[22] J. He, Y. W. Li, J. M. Guerrero, F. Blaadjerg, and J. C. Vasquez, "An islanding microgrid power sharing approach using enhanced virtual impedance control scheme," *IEEE Trans. Power Electron.*, vol. 28, no. 11, pp. 5272–5282, Nov. 2013.
[23] K. D. Brabandere, B. Bolsens, J. V. Keybus, A. Woyte, J. Driesen, and R. Belmans, "A voltage and frequency droop control method for parallel inverters," *IEEE Trans. Power Electron.*, vol. 22, no. 4, pp. 1107–1115, Jul. 2007.
[24] J. Hu, J. Zhu, D. G. Dorrell, and J. M. Guerrero, "Virtual flux droop method—A new control strategy of inverters in microgrids," *IEEE Trans. Power Electron.*, vol. 29, no. 9, pp. 4704–4711, Sep. 2014.
[25] H. Mahmood, D. Michaelson, and J. Jiang, "Accurate reactive power sharing in an islanded microgrid using adaptive virtual impedances," *IEEE Trans. Power Electron.*, vol. 30, no. 3, pp. 1605–1617, Mar. 2015.
[26] A. Urtasun, P. Sanchis, and L. Marroyo, "Limiting the power generated by a photovoltaic system," in *Proc. Multi-Conf. Syst., Signals Devices*, 2013, pp. 1–6.
[27] Z. M. Dalala, Z. U. Zahid, and J.-S. Lai, "New overall control strategy for small-scale WECS in MPPT and stall regions with mode transfer control," *IEEE Trans. Energy Conver.*, vol. 28, no. 4, pp. 1082–1092, Dec. 2013.
[28] Y. Yang and F. Blaabjerg, "Synchronization in single-phase grid-connected photovoltaic systems under grid faults," in *Proc. Int. Symp. Power Electron. Distrib. Gener. Syst.*, 2012, pp. 476–482.
[29] J. Rocabert, A. Luna, F. Blaabjerg, and P. Rodriguez, "Control of power converters in AC microgrids," *IEEE Trans. Power Electron.*, vol. 27, no. 11, pp. 4734–4749, Nov. 2012.
[30] S. G. Jorge, J. A. Solsona, and C. A. Busada, "Control scheme for a single-phase grid-tied voltage source converter with reduced number of sensors," *IEEE Trans. Power Electron.*, vol. 29, no. 7, pp. 3758–3765, Jul. 2014.
[31] S. Golestan, M. Ramezani, J. M. Guerrero, and M. Monfared, "*dq*-frame cascaded delayed signal cancellation-based PLL: Analysis, design, and comparison with moving average filter-based PLL," *IEEE Trans. Power Electron.*, vol. 30, no. 3, pp. 1618–1632, Mar. 2015.
[32] P. Sanchis, L. Marroyo, and J. Coloma, "Design methodology for the frequency shift method of islanding prevention and analysis of its detection capability," *Prog. Photovoltaics*, vol. 13, no. 5, pp. 409–428, 2005.
[33] M. Ross, C. Abbey, Y. Brissette, and G. Joos, "Photovoltaic inverter characterization testing on a physical distribution system," in *Proc. IEEE Power Energy Soc. Gen. Meet.*, 2012, pp. 1–7.
[34] J. Pascual, P. Sanchis, and L. Marroyo, "Implementation and control of a residential electrothermal microgrid based on renewable energies, a hybrid storage system and demand side management," *Energies*, vol. 7, no. 1, pp. 210–237, 2014.
[35] P. O. Kriett and M. Salani, "Optimal control of a residential microgrid," *Energy*, vol. 42, no. 1, pp. 321–330, 2012.
[36] A. R. Bergen, *Power Systems Analysis*. Englewood Cliffs, NJ, USA: Prentice-Hall 1986.
[37] A. Urtasun, P. Sanchis, and L. Marroyo, "RMS voltage control with harmonic compensation for parallel-connected inverters feeding non-linear loads," in *Proc. Int. Symp. Circuits Syst.*, 2014, pp. 1179–1182.
[38] J. M. Guerrero, J. Matas, L. G. de Vicuña, M. Castilla, and J. Miret, "Decentralized control for parallel operation of distributed generation inverters using resistive output impedance," *IEEE Trans. Ind. Electron.*, vol. 54, no. 2, pp. 994–1004, Apr. 2007.
[39] E. A. A. Coelho, P. C. Cortizo, and P. F. D. Garcia, "Small signal stability for single phase inverter connnected to stiff ac system," in *Proc. IEEE Ind. Appl. Conf.*, 1999, no. 4, pp. 2180–2187.
[40] A. Urtasun, P. Sanchis, and L. Marroyo, "Comparison of linear and small-signal models for inverter-based microgrids," in *Proc. Australasian Univ. Power Eng. Conf.*, to be published.
[41] T. Messo, J. Jokipii, J. Puukko, and T. Suntio, "Determining the value of DC-link capacitance to ensure stable operation of a three-phase photovoltaic inverter," *IEEE Trans. Power Electron.*, vol. 29, no. 2, pp. 665–673, Feb. 2014.
[42] S. G. Tesfahunegn, P. J. S. Vie, O. Ulleberg, and T. M. Undeland, "A simplified battery charge controller for safety and increased utilization in stand-alone PV applications," in *Proc. Conf. Clean Electr. Power*, 2011, pp. 137–144.
[43] E. Barklund, N. Pogaku, M. Prodanovic, C. Hernandez-Aramburo, and T. C. Green, "Energy management in autonomous microgrid using stability-constrained droop control of inverters," *IEEE Trans. Power Electron.*, vol. 23, no. 5, pp. 2346–2352, Sep. 2008.

Andoni Urtasun (S'11) was born in Pamplona, Spain, in 1987. He received the M.Sc. degree in electrical engineering from the Public University of Navarre, Pamplona, Spain, and also from the Institut National Polytechnique de Toulouse, Toulouse, France, both in 2010. He is currently working toward the Ph.D. degree at the Public University of Navarre.

In 2010, he joined the Electrical Engineering, Power Electronics and Renewable Energy Research Group, Public University of Navarre. His research interests include power electronics and renewable energies.

Ernesto L. Barrios (S'12) was born in Pamplona, Spain, in 1988. He received the B.Sc. and M.Sc. degree in electrical engineering from the Public University of Navarre, Pamplona, Spain, in 2009 and 2012, respectively.

In 2011, he joined the Electrical Engineering, Power Electronics and Renewable Energy research group (INGEPER), Public University of Navarre, where he is currently pursuing his Ph.D. His main research interests include high frequency magnetics, wide bandgap power semiconductor devices and power converters for renewable energies, particularly for photovoltaics and fuel cells.

Pablo Sanchis (M'03–SM'12) received the M.Sc. degree in management and business administration, and the M.Sc. and Ph.D. degrees in electrical engineering all from the Public University of Navarra, Pamplona, Spain, in 1994, 1995, and 2002, respectively.

From 1996 to 1998, he was a Guest Researcher at the Delft University of Technology, The Netherlands, on the field of control of electric machines. In 1998, he joined the Department of Electrical and Electronic Engineering, Public University of Navarra, where he is currently an Associate Professor. He is also the Director of the Renewable Energies Space and the Vice-Dean of the College of Engineering of this university. He has been involved in many research projects mainly in cooperation with industry. His research interests include renewable energies, power electronics, hydrogen technologies, electric grid integration, and electric microgrids.

Dr. Sanchis is a Member of the IET, the CIGRE, and the Spanish Hydrogen Association (AEH2).

Luis Marroyo (M'04) received the M.Sc. degree in electrical engineering from the University of Toulouse, Toulouse, France, in 1993, and the Ph.D. degree in electrical engineering from the Universidad Pública de Navarra, Pamplona (UPNA), Spain, in 1997, and also from the LEEI-ENSEEIHT INP, Toulouse, in 1999.

From 1993 to 1998, he was an Assistant Professor at the Department of Electrical and Electronic Engineering, UPNA, where he is currently working as an Associate Professor, from 1998. He is the Head of the INGEPER Research Group. He has been involved in more than 60 research projects, mainly in cooperation with industry, he is the Coinventor of 11 international patents, and a Coauthored of more than 70 papers in international journals and conferences. His research interests include power electronics, grid quality, and renewable energy.